Chapter 4

Event Selection

Of all that is written I love only what a man has written with his blood.

F. Nietzsche, "Also Sprach Zarathustra"

This chapter contains a detailed description of the selection of the reaction (2.7) events with the DØ detector for both the electron and muon channels:

$$p\bar{p} \rightarrow e^+e^-\gamma; \tag{4.1}$$

$$p\bar{p} \rightarrow \mu^+\mu^-\gamma. \tag{4.2}$$

All available data from the first physics run of the DØ detector (run Ia, 1992–1993) at $\sqrt{s} = 1.8$ TeV was used in these analyses. The total integrated luminosity delivered to DØ by the Tevatron for this run was 27.8 pb^{-1} (see sec. 3.6.7 for details of luminosity calculations). The accepted luminosity, however, was about a factor of two smaller, 14.9 ± 1.8 pb^{-1}. The main reason for this inefficiency is a 27% dead time due to the Main Ring injection and microblanking (see sec. 3.6.2) forced by the fact that the Main Ring of the accelerator passes through the DØ detector. The other contributions to the total 46% dead time are as follows: DAQ system dead time — 8% (see sec. 3.6), HV trips — 6% (see sec. 3.6.6), run startup — 2%, and changing of the triggers — 3%. The integrated luminosities for the specific high p_T triggers used for selection of the electron and muon events are somewhat lower due to corrections for the bad and special runs (see sec. 4.2 and 4.3).

The raw data collected on magnetic tapes (Exabyte format) was reconstructed by version 11 of the standard reconstruction (DØRECO) program [57] — the latest one available for the run Ia (see sec. 3.6.5). Various energy corrections were introduced during the reconstruction. These corrections are necessary due to the different high-voltage and other environmental parameters in the physical run and during the liquid argon calorimeter test beam calibration [72]. Beyond this, we used additional electromagnetic and jet energy corrections [70] before applying specific cuts to the data. These corrections further tune the energy scale of the calorimeter, take into account the invisible energy in the hadronic jets (thus improving the $\not\!\!E_T$ resolution), and adjust the Z mass to the LEP value of 91.2 GeV [9] (see sec. 3.3.7). In what follows, we will use the corrected energies for defining the cuts unless otherwise stated.

4.1 Particle Identification

The selection of the reactions (4.1), (4.2) relies very much on a correct and trustworthy identification of the final state particles: electrons, muons, and photons. In this section we discuss the algorithms used to identify these three types of particles. Most of the algorithms are standard within the DØ Collaboration and are used in various physics analyses. Modifications to these standard algorithms are emphasized in the appropriate sections.

4.1.1 Electron Identification

Since the DØ detector does not have a central magnetic field, the initial stage of electron identification is based on EM calorimeter information. We use tracking information in the CD (see sec. 3.4) to distinguish between electrons and photons. This approach is an alternative to that used in the detectors with a magnetic field where it is possible to measure track curvature and momentum to energy ratio, P/E, and use them for particle identification. For the case of the DØ detector the absence of P/E information is compensated for by fine segmentation of the EM calorimeter, dE/dx measurements in the CDC and FDC (see sec. 3.4), and by the TRD information (see sec. 3.4.2). The major sources of background to electrons at DØ are converted photons and QCD jets with a high fraction of electromagnetic energy. Because of the absence of the magnetic field we are not able to distinguish between electrons and positrons, so in what follows we will talk about electrons, or e's, implying particles of both signs.

The reconstruction program loosely labels an electromagnetic cluster as an electron if there is a track in the "cone" of the width $\approx 0.1 \times 0.1$ in $\theta - \phi$ space, which points from the interaction vertex to the center of gravity of the cluster. (In what follows such a cone will be called the *tracking road*.) Information about the cluster matching such a track is stored in PELC ZEBRA bank (see sec. 3.6.5), while a cluster which fail this requirement is associated with a photon and stored in PPHO bank. Of course, such an assignment is rather poor, and thus both banks are heavily contaminated by background.

However, the DØ finely segmented calorimeter (see sec. 3.3) allows us to suppress these backgrounds drastically by means of a thorough multidimensional analysis of the longitudinal and transverse profiles of the electromagnetic showers. Shower shapes are in general different for the case of an $e^+e^-/\gamma\gamma$ pair and a single electron/photon with the same total energy due to fluctuations of the shower origin for each particle. One would expect a shower from a converted photon/π^0 to develop earlier, because the probability of the initial interaction in the first layer of the calorimeter for two particles is twice as high as that for a single one. At the same time, unlike measurements based on the P/E ratio, the DØ electron identification algorithm is not very sensitive to δ-ray electrons (i.e. electrons kicked out of atoms) and electrons which radiate photons in the material before the calorimeter via *bremsstrahlung*, because secondary electrons and photons generally have much lower energy than the parent particle and thus do not significantly change the shower energy profile.

A further improvement of the electron identification can be achieved by measuring the ionization (dE/dx) along a track in the CD. However, the efficiency of this algorithm for electrons is not very high (about 85% per electron for background rejection factor of 2), so we do not use the dE/dx information in this analysis due to the very limited statistics of the signal events. The TRD information (see sec. 3.4.2) is not used for similar reasons.

The analysis of the shower profile is done by the so-called *H-matrix* algorithm [109]. It analyzes the observed energy depositions in different cells of an electromagnetic cluster found by the reconstruction program (see sec. 3.6.5). In order to compare the energy profile of a particular cluster with the expectations, a 41×41 covariance matrix is built from the energy depositions for the electrons in the Monte Carlo sample. The inverse of this matrix is called the H-matrix. A χ^2-like function is then calculated in a standard way on a cluster-by-cluster basis using the H-matrix as an error matrix. This χ^2-like function is therefore a quantitative measure of the probability that the cluster is due to a single electron/photon. Optimum cuts on the H-matrix χ^2 for electron identification were determined using the electron and pion test-beam data [110].

All cuts for the electron selection which we are going to discuss were studied using the background-subtracted $Z \to ee$ event sample collected in the same run. The efficiency of a certain cut was obtained by comparing the total number of events in the Z-peak before and after the cut was applied. The efficiency for a set of cuts was calculated in a similar way (which correctly takes into account the correlations between cuts). The values of the cutoff parameters were chosen to optimize the signal-to-background ratio in the background-contaminated $Z \to ee$ sample while retaining relatively high efficiency for the signal [111].

The basic set of cuts is summarized in Table 4.1. The efficiency as a function of cutoff parameters is shown in Fig. 4.1 [111]. The cuts used in the analysis are indicated by the arrows in the plot. The cuts are somewhat different for the CC and EC (see sec. 3.3 for the calorimeter description) because of the different amount of material in front of the central and end calorimeters which results in different multiple scattering and conversion probabilities for electrons and photons hitting the CC and EC.

The H-matrix χ^2 cut is a likelihood cut on the cluster energy profile. It has a higher cutoff in the EC because of the larger electromagnetic shower fluctuations in the forward region. The electromagnetic fraction cut accepts only the clusters with at least 90% of the energy being deposited in the electromagnetic layers of the calorimeter. The isolation cut requires the clusters to be rather narrow. The definition of the isolation is as follows:

$$\mathrm{ISO} = \frac{E^{tot}(\Delta R = 0.4) - E^{EM}(\Delta R = 0.2)}{E^{EM}(\Delta R = 0.2)}. \tag{4.3}$$

Here $E(\Delta R)$ is the energy deposited in a cone of radius ΔR in $\eta - \phi$ space.

Cut description	CC		EC	
	Cutoff	ε	Cutoff	ε
H-matrix χ^2	< 100	0.930 ± 0.011	< 200	0.987 ± 0.022
EM fraction	> 0.90	0.995 ± 0.005	> 0.90	0.995 ± 0.005
Isolation	< 0.10	0.970 ± 0.008	< 0.10	0.982 ± 0.023
Loose cuts (all above)		0.902 ± 0.013		0.971 ± 0.029
Track in road	see text	0.879 ± 0.022	see text	0.820 ± 0.024
Track match	$< 10\sigma$	0.977 ± 0.006	$< 10\sigma$	0.881 ± 0.023
Tight cuts (all above)		0.781 ± 0.023		0.708 ± 0.034

Table 4.1: Definitions and efficiencies [111] for the electron identification cuts in the central and end calorimeters.

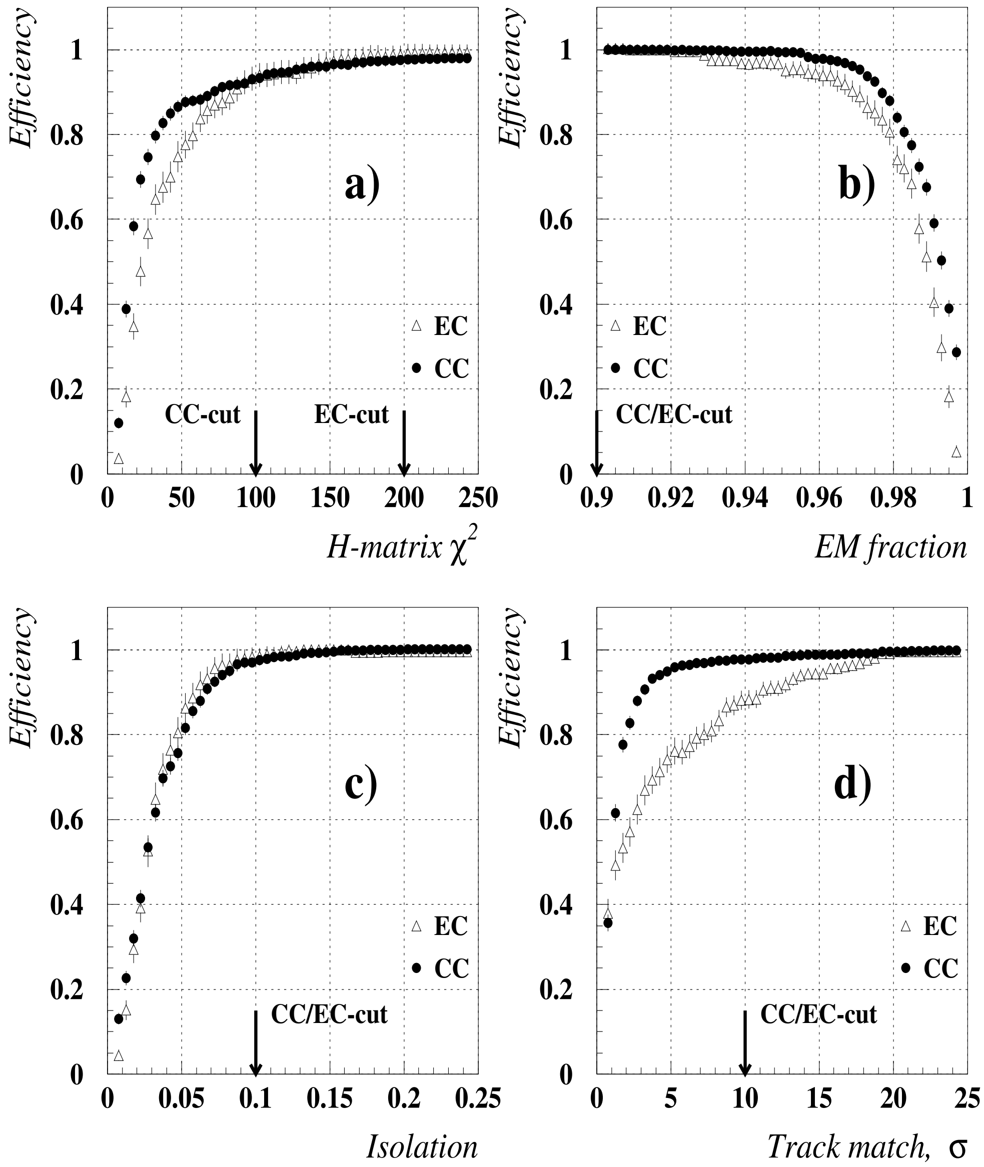

Figure 4.1: Efficiencies for various electron identification cuts: a) H-matrix χ^2 cut; b) electromagnetic fraction cut; c) isolation cut; d) track match significance cut. Dots — central calorimeter; open triangles — end calorimeters. Arrows show the actual values of cutoff parameters used in this analysis.

This cone is drawn from the event vertex to the center of gravity of the electromagnetic cluster. The smaller the value of ISO, the more compact a cluster is. Since an electromagnetic shower should be fully contained in the $\Delta R = 0.2$ cone, this cut selects electrons (photons) which are well separated from other particles (i.e. *isolated*).

The set of these three cuts is called the *loose electron/photon* selection criterion. If in addition the cluster was reconstructed as an electron by DØRECO (see above) and matches within 10σ one of the reconstructed central tracks, we refer to it as to passing the *tight electron* cut. The parameter σ in the track match definition is a combined error of tracking and cluster position reconstruction due to multiple scattering, vertex z-position mismeasurements, etc.

Because of the small signal cross section, and a low expected background (see sec. 4.5), we optimize the selection efficiency by requiring only one electron to pass the tight electron cut, while for the second it is sufficient to satisfy only the loose selection criterion. The motivation for this less stringent requirement is a significant tracking inefficiency which results in $\approx 13\%$ of the electrons to be placed into the PPHO (photon) banks.

The overall electron identification efficiency for two electrons was estimated using the ratio of tight-loose (N_{tl}) to tight-tight (N_{tt}) $Z \to ee$ events. This ratio was measured to be $1:3$ which is consistent with the tracking efficiency (measured by several other techniques), $\varepsilon_t = 84 - 87\%$ (see Table 4.1):

$$\frac{N_{tl}}{N_{tt}} = \frac{2\varepsilon_t(1-\varepsilon_t)}{\varepsilon_t^2} = 2\left(\frac{1}{\varepsilon_t} - 1\right). \tag{4.4}$$

Identification efficiencies for both electrons in the CC and both electrons in the EC were found to be:

$$\varepsilon^{ee}_{CC} = 0.64 \pm 0.02, \quad \varepsilon^{ee}_{EC} = 0.56 \pm 0.03. \tag{4.5}$$

Efficiencies for the CC–EC topologies were also calculated and used in the DØBAUR Monte Carlo (see sec. 3.7).

4.1.2 Photon Identification

Photon identification is similar to electron identification in the DØ detector. We require an electromagnetic cluster to have no track in the 0.1×0.1 cone in $\theta - \phi$ space (i.e. to belong to the PPHO bank). Beyond this we require the cluster to satisfy loose electron/photon selection criteria (see sec. 4.1.1). Thus, the identification efficiency for a photon which belongs to the PPHO bank is given by the "loose cuts" line of the Table 4.1.

However, a certain fraction of photons are reconstructed as electrons (and thus are misplaced into PELC banks) due to conversions in the material in front of the CDC or FDC and due to the overlap of random tracks with the electromagnetic cluster associated with the photon. The conversion probability, P_c, was calculated [112] using the DØGEANT [103] detector simulation program. P_c as a function of the photon pseudorapidity measured in the calorimeter (η_{det}) is shown in Fig. 4.2 (a) for the case of the interaction vertex in the center of the detector ($\eta_{det} = \eta$). It was then multiplied by the tracking efficiency in order to get η-dependent probability of photon losses due to conversions. This probability was used in the Monte Carlo calculations of the theoretical cross section (see sec. 3.7).

The probability of a random track overlap was calculated using real $Z \to ee$ data. The electrons in this sample have a similar pseudorapidity distribution as one would expect for photons in the $Z\gamma$ production (see Fig. 2.6). We calculated the probability of observing a random track from the underlying

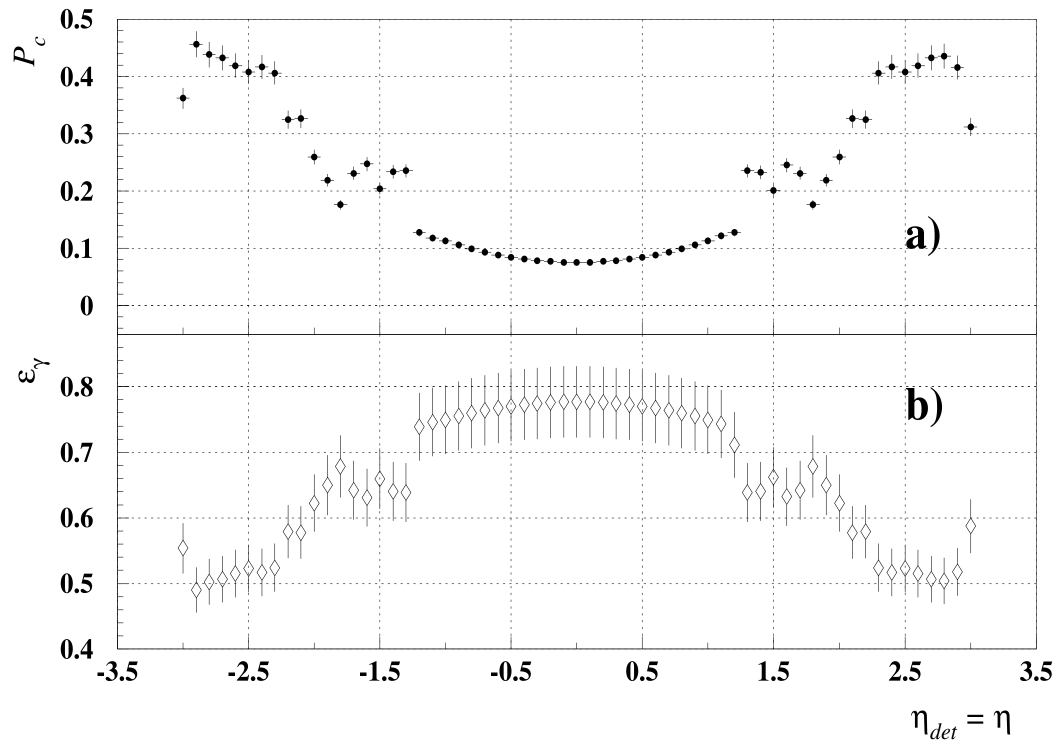

Figure 4.2: a) η-dependent probability for photon conversion (P_c) in the material in front of the CDC/FDC; b) η-dependent efficiency of the photon identification (ε_γ) for high p_T photons. Error bars show a 5% systematic uncertainty in the conversion probability calculations, and an overall 7% systematic uncertainty in the efficiency estimations.

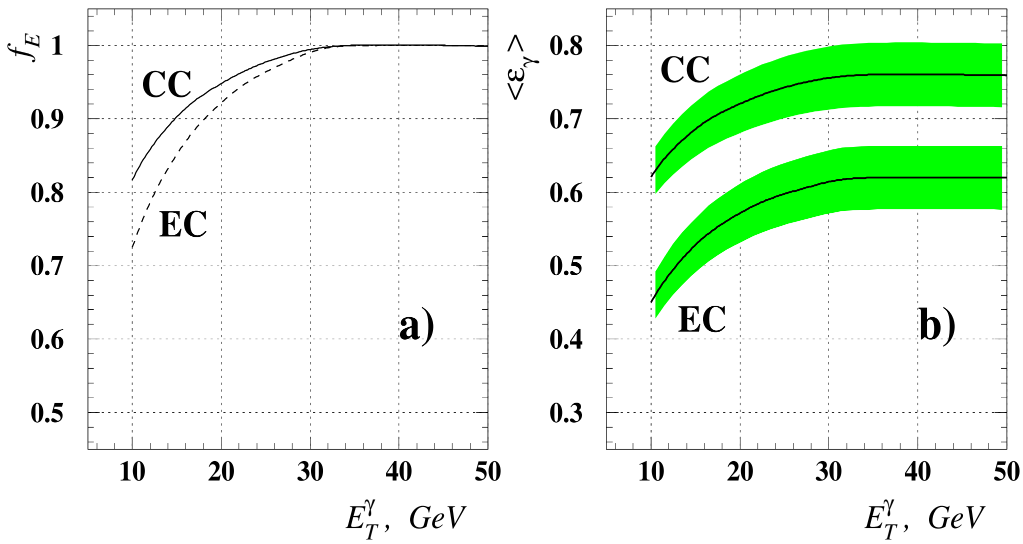

Figure 4.3: a) E_T^γ-dependent correction factor (f_E) for the H-matrix cut efficiency in the CC (solid line) and EC (dashed line); b) E_T^γ-dependent photon identification efficiency, averaged in η_γ, ($\langle\varepsilon_\gamma\rangle$) for CC (upper) and EC (lower); the shadowed bands represent $\pm 7\%$ systematic uncertainty.

event in a random cone of $\theta \times \phi \approx 0.1 \times 0.1$ size — the same as used in DØRECO's coarse electron/photon identification algorithm. The cones have the same η_{det} as electrons in the $Z \rightarrow ee$ sample, but the ϕ-coordinate was chosen randomly. The efficiency due to a random track overlap was found to be $94 \pm 1\%$ in CC and $85 \pm 1\%$ in EC, the latter being lower due to the higher density of tracks in the forward region.

The η-dependent efficiency of the photon identification for the $\eta_{det} = \eta$ case after applying loose electron cuts and taking into account conversions and random track overlap losses is shown in Fig. 4.2 (b).

The efficiency of the H-matrix cut in Table 4.1 was calculated for electromagnetic clusters with $E_T > 25$ GeV. For photons we would like to go much lower in transverse energy, so an additional E_T-dependent correction to the efficiency must be introduced. The correction factor as a function of the photon transverse energy was measured in the test beam [110]. It is shown in Fig. 4.3 (a) for the CC (solid line) and EC (dashed line). The overall E_T dependent photon identification efficiency in the CC and EC after integration over a typical η distribution (see Fig. 2.6) is shown in Fig. 4.3 (b).

After taking into account the E_T-dependent corrections, the average efficiencies for photons produced in the reaction (2.7) in the central and forward regions are found to be 67% and 52%, respectively. The overall error in the photon identification efficiency calculations is 7% and is dominated by the systematic errors in f_E and the conversion probability.

4.1.3 Muon Identification

The basic algorithms used for the muon identification were developed and studied in great detail for the top-quark search in the reaction $p\bar{p} \rightarrow t\bar{t} \rightarrow e\mu + jets$ [95, 113] as well as for other physics analyses which involve muons. The efficiencies of the muon identification cuts were calculated using the $W \rightarrow \mu\bar{\nu}$ and $Z \rightarrow \mu\mu$ data and Monte Carlo samples.

The analysis of the reaction (4.2) was restricted to the CF muon system only (see sec. 3.5 for notations) because of the present low efficiency of the forward EF system and higher background from accidentals in the forward region. The muons in the reaction (4.2) are expected to be mostly central, so this restriction does not decrease the acceptance significantly.

Cut description	Cutoff definition	ε
Cosmic rejection cuts		
No back-to-back muon tracks or hits		0.84 ± 0.01
No cross-octant muon tracks		0.99 ± 0.01
Vertex consistence	$d_{3D} < 22.0$ cm	0.99 ± 0.01
Muon quality cuts		
A-layer hits requirement		0.86 ± 0.01
Number of layers hit	$N_L \geq 2$	0.95 ± 0.03
Muon track quality	$IFW4 \leq 1$	0.99 ± 0.01
CD track match	$\Delta\phi < 0.25,\ \Delta\theta < 0.30$	0.95 ± 0.02
Calorimeter MIP deposition	$E > 1.0$ GeV	0.99 ± 0.01
Isolation	$\Delta R(\mu - jet) > 0.5$	0.96 ± 0.02
Cuts common for both muons	All above, per 2μ	0.55 ± 0.04
Additional cuts which only one out of two muons must pass		
Hits in all three layers		0.97 ± 0.03
Fiducial cut	$\int B\, dl > 1.9$ Tm	0.97

Table 4.2: Definitions and efficiencies for the muon identification cuts in the central muon system.

The basic cuts used for the muon identification are summarized in Table 4.2. Three separate cuts were applied to suppress the cosmic ray background. First of all, we reject the tracks and hits which are back-to-back in the $\theta - \phi$ plane (i.e. with both $\Delta\theta$ and $\Delta\phi$ greater than 170°). Second, the tracks which cross octant boundaries (see sec. 3.5) are discarded because they can not come from the interaction vertex. Finally, we require the three-dimensional impact parameter, d_{3D} (i.e. the closest distance from the muon track to the interaction vertex) to be less than 22 cm, which ensures the consistency of the track with the vertex and aids significantly in cosmic rejection. These cuts were studied and optimized by analyzing single muon and cosmic ray tracks with $p^\mu > 7$ GeV/c.

Several quality criteria are used to ensure that only good tracks are kept. We require at least two out of three muon layers to have hits consistent with the track. Among these two layers the innermost A-layer is always required to be hit. The absence of hits in one of the outer layers is usually due to the "holes" in the muon system coverage, and such events were "verified" by eye-scanning of the events.

The standard muon reconstruction code of DØRECO returns a special flag, $IFW4$, which contains information on the "goodness" of the track fit. Several parameters, like the χ^2 of the fit in both the bend and the non-bend views, are used to set this flag. If the track fails a certain requirement, DØRECO adds 1 to the value of $IFW4$. Thus the flag is equal to 0 for "golden" muons; all muon candidates with $IFW4 > 2$ are discarded by the reconstruction program. We further tightened this cut and accepted only the muons with $IFW4 \leq 1$. Such a cut reduces number of fake muons significantly.

Finally, we require a matching track for the muon in the CD, and a minimum ionizing particle (MIP) energy deposit in the calorimeter along the muon track. Furthermore, we accept only muons isolated from jets with $E_T^j > 10$ GeV ($\Delta R_{\mu j} > 0.5$) to reject secondary muons from decaying hadrons in jets. This cut also reduces the background from muons faked by jets due to the energy leakage into the muon system in the areas with a low amount of the calorimeter material.

The cuts discussed above are combined to define the *loose muon* selection criterion. Both muons of reaction (4.2) must pass the loose cuts. In addition we require two cuts which only one of the muons must satisfy. The first of these is the requirement of a three-layer track. The second one is a fiducial volume cut which improves the momentum reconstruction of the muon. We require one of the muons to traverse a field integral $\int B\,dl > 1.9$ Tm. These two additional cuts are applied independently, so different muons of the pair may satisfy each of them. It was checked using $Z \to \mu\mu$ data that the loose selection criteria efficiencies are not correlated with these two extra requirements. The momentum resolution for the low $\int B\,dl$ region ($\int B\,dl < 1.9$ Tm) was studied in detail and parameterized by the following formula:

$$\left(\frac{\sigma(\frac{1}{p_\mu})}{\frac{1}{p_\mu}}\right)^2 = 0.18^2 + (0.0175 \cdot p_\mu[\mathrm{GeV}/c])^2, \tag{4.6}$$

which should be compared with (3.6) for high $\int B\,dl$ muons. Such a degraded resolution in the low $\int B\,dl$ region does not affect the cross sections calculated with the DØBAUR Monte Carlo program within the systematic uncertainty of the calculations (see sec. 3.7).

The overall efficiency of the identification of a pair of muons passing tight selection criteria was calculated using the $Z \to \mu\mu$ samples from data and from the DØGEANT Monte-Carlo. It was found to be:

$$\varepsilon_{CF}^{\mu\mu} = 0.54 \pm 0.04. \tag{4.7}$$

4.2 Selection of $p\bar{p} \rightarrow ee\gamma$ Events

Now, after discussing the particle identification, we will address the actual algorithms used in the selection of the events of reaction (4.1). Beyond the standard electron and photon quality cuts we introduce additional kinematical and fiducial requirements for the final state particles:

$$\begin{gathered} |\eta_{det}^{e/\gamma}| \leq 1.1 \text{ or } 1.5 \leq |\eta_{det}^{e/\gamma}| \leq 2.5; \\ p_T^e > 25 \text{ GeV/c}, \quad p_T^\gamma > 10 \text{ GeV/c}; \\ \Delta R_{e^\pm\gamma} > 0.7. \end{gathered} \tag{4.8}$$

Here and in what follows η_{det} is the pseudorapidity of an object in the detector frame with a vertex at $z = 0$ (in the center of the detector). It coincides with the physical pseudorapidity, η, when the vertex of the interaction also has $z = 0$. We use η_{det} for the acceptance cuts because they are determined by the geometry of the detector. We also reject events which have an electron or photon in the region of $1.1 < |\eta_{det}| < 1.5$ where the amount of the EM calorimetry material is small (see sec. 3.3) and the EM energy measurement is not reliable. The upper limit for the electron or photon pseudorapidity of 2.5 is motivated by a large amount of the material in front of the FDC (see sec. 3.4.4) beyond this pseudorapidity threshold and by the large particle flux in the very forward region which diminishes the tracking efficiency. Furthermore, the conversion probability for such a forward photon is very high (see Fig. 4.2), as is the random track overlap probability.

Finally, the transverse momentum cuts for the electrons were chosen based on the optimization of the signal to background for the $Z \to ee$ sample. The transverse momentum cut for the photon is motivated by the efficiency of the H-matrix cut which is not only low but also not well understood for electromagnetic clusters with $E_T < 10$ GeV. Therefore, lowering the photon p_T threshold to a value below 10 GeV/c is very problematic.

Based on the set of cuts listed in (4.8) we choose the ELE_2_MAX Level 2 trigger for the selection of reaction (4.1) candidates. This trigger corresponds to the EM_2_MED Level 1 trigger, which requires transverse energy depositions greater than 7 GeV in at least two trigger towers of the EM calorimeter. The Level 2 trigger further requires two electromagnetic clusters with the transverse energy greater than 20 GeV which pass certain isolation and quality cuts. Neither trigger was prescaled during run Ia. The integrated luminosity for the ELE_2_MAX trigger (after correction for bad and special runs) is 13.9 ± 1.7 pb^{-1} (see sec. 3.6.7 for details of the luminosity calculations). The efficiency of the trigger for the offline cuts of $p_T > 25$ GeV/c for two electrons was calculated using the $Z \to ee$ event sample. It was found to be:

$$\varepsilon_{L1+L2} = 0.98 \pm 0.01. \tag{4.9}$$

The efficiency of the fiducial (η) cuts (or the acceptance) depends on the actual pseudorapidity distribution of the photons and electrons. It was calculated by the DØBAUR Monte-Carlo program (see sec. 3.7). For the SM case the fiducial cuts are 53% efficient. This efficiency is slightly higher for the non-zero anomalous couplings because the pseudorapidity distribution of the final state particles is more central in this case (the DØBAUR Monte Carlo describes the efficiency increase correctly). The overall efficiency and cross section for the reaction (4.1) within the set of cuts (4.8) for the SM case are:

$$\varepsilon_{SM} = 0.20 \pm 0.02; \tag{4.10}$$

$$\sigma_{SM} \cdot \varepsilon_{SM} = 0.225 \pm 0.025 \text{ pb}. \tag{4.11}$$

We started the event selection from the standard $Z \to ee$ sample with very loose cuts imposed. The sample was selected from the so-called RGE offline stream which contains all events which pass at least one of a large number of different offline filters. (The RGE acronym stands for "Really Good Events".) This data stream basically contains all the events interesting to different physics groups doing a broad spectrum of analyses. The $Z \to ee$ sample was selected by a standard W/Z-finder package [114] which requires at least two electromagnetic clusters with uncorrected transverse energy (E_T^{uncor}) greater than 15 GeV which pass some cluster quality cuts, significantly looser than the set listed in Table 4.1. The additional offline energy corrections are less than 10%, so the $E_T^{uncor} > 15$ GeV requirement is guaranteed to be less stringent than the $E_T > 17$ GeV cut. Since only two clusters are required to pass the E_T cut, the photon transverse energy is unrestricted if we require both electrons to have $E_T > 17$ GeV. However, we superimpose a loose cut on the third electromagnetic cluster ($E_T > 5$ GeV) in order to get rid of soft and fake photons (in practice, low-energy electromagnetic clusters found by the reconstruction program). We also require at least one of the clusters to belong to PELC bank and to have a track match significance $< 10\sigma$. The starting sample after these (very loose) requirements consists of 77 events.

Cut description	No. of survived events
Starting sample	77
$\chi^2 < 100$ (CC), 200 (EC)	25
EM fraction > 0.90	25
ISO < 0.10	21
Fiducial cuts	15
μ-blanking	13
$p_T^e > 25$ GeV/c	10
ELE_2_MAX trigger	10
$\Delta R_{min}^{e\gamma} > 0.7$	8
$p_T^\gamma > 10$ GeV/c	4

Table 4.3: Number of $ee\gamma$ candidates passing different selection criteria.

After applying the H-matrix cuts (see Table 4.3), the sample is reduced to 25 events. All events pass the EM-fraction cut; 4 events fail the ISO < 0.10 cut on the electron/photon isolation. Thus, after particle identification requirements on all three final state particles we get only 21 events in the sample. Another 6 events fail the fiducial cuts (4.8); 2 events have a microblanking bit set, which means that they were taken during the Main Ring activity, and are thus unreliable (see sec. 3.6.2). After requiring both electrons to pass the $p_T > 25$ GeV/c requirement, we end up with 10 events. All of them pass the Level 2 trigger requirements; 2 events fail the separation cut. Among the remaining 8 events, 4 have a photon with transverse energy below 10 GeV (see Table 4.3).

The final sample consists of 4 events; 3 of them have two "tight" electrons, and one has one "tight" and one "loose" electron, which is exactly what one would expect from the DØ tracking efficiency (see sec. 4.1.1). The "loose" electron for that one event (58796/247, see Table. 4.4) does not have an associated track and thus belongs to the PPHO class. However, there is no ambiguity in associating one of the two PPHO banks with the electron. Eye-scanning of the event 58796/247 clearly shows a trace of hits in the CDC (see sec. 3.4.3) along the line from the vertex to one of the PPHO clusters. There are no

Particle	Type	p_T	η	ϕ	N_j/E_T^j	$\not{E}_T$	$M_{ee\gamma}$	M_{ee}	$\Delta R_{e\gamma}$
Run/Event: 58486/212									
e_1	tight	53.8	-1.86	6.03					2.96
e_2	tight	43.7	-1.85	2.30	1/26.9	5.5	159.5	92.8	3.51
γ		12.2	0.76	4.65					
Run/Event: 58796/247									
e_1	tight	29.3	-0.20	2.91					1.13
e_2	loose	36.0	0.47	0.14	0	6.3	90.5	67.5	2.64
γ		18.1	-0.54	3.99					
Run/Event: 63120/16499									
e_1	tight	28.3	1.82	1.34					2.40
e_2	tight	26.5	0.13	4.08	0	4.4	90.0	74.9	1.73
γ		11.5	0.26	5.81					
Run/Event: 64425/1906									
e_1	tight	35.2	-0.63	3.86					2.31
e_2	tight	30.3	0.36	0.41	0	7.3	86.4	73.0	1.28
γ		12.2	0.06	1.66					

Table 4.4: Parameters of the final $p\bar{p} \to Z\gamma \to ee\gamma$ candidates. Unit for masses is GeV/c^2; for transverse momenta — GeV/c; for E_T and $\not{E}_T$ — GeV.

associated hits along the line to the other PPHO cluster. Moreover, the real photon is close to the "tight" electron in the event as one would expect for a decay event, while the "loose" electron is almost back-to-back with the tight electron. The $\not{E}_T$ in all four candidates is very small, as one would expect for $ee\gamma$ events. Only one out of four events has a jet with transverse energy above 7 GeV, which is in agreement with the k-factor of 1.34 (see sec. 2.3.4).

The parameters of the four observed candidates are listed in Table 4.4. Transverse energy of the photon, masses of the ee-pair and $ee\gamma$ system, as well as the minimum separation for the candidate events are shown in Fig. 4.4. The SM predictions obtained from the Monte Carlo with fast detector simulation are shown in the same plots as histograms. It is clear from the table and from the plots that three events can be naturally associated with the decay mechanism, while one event with high invariant mass of the $Z\gamma$ system is a production event. The $ee\gamma$ invariant mass for this event is somewhat higher than one would expect from SM, but with such a limited number of candidates such a difference is not statistically significant. The anomalously large ΔR in the same event can be explained by the presence of a hadronic jet in the event, which boosts the whole $Z\gamma$ system.

The display of the production event, produced with the standard DØ event viewer, PIXIE [115], is shown in Figs. 4.5 and 4.6. The top plot in the first figure is an $r-z$-view of the event, integrated and the folded over ϕ. Two EM clusters corresponding to electrons are in the North EC (left side of the figure). The tracks pointing toward these clusters are clearly seen in the North FDC. They point to the vertex (small cross on the z-axis) which

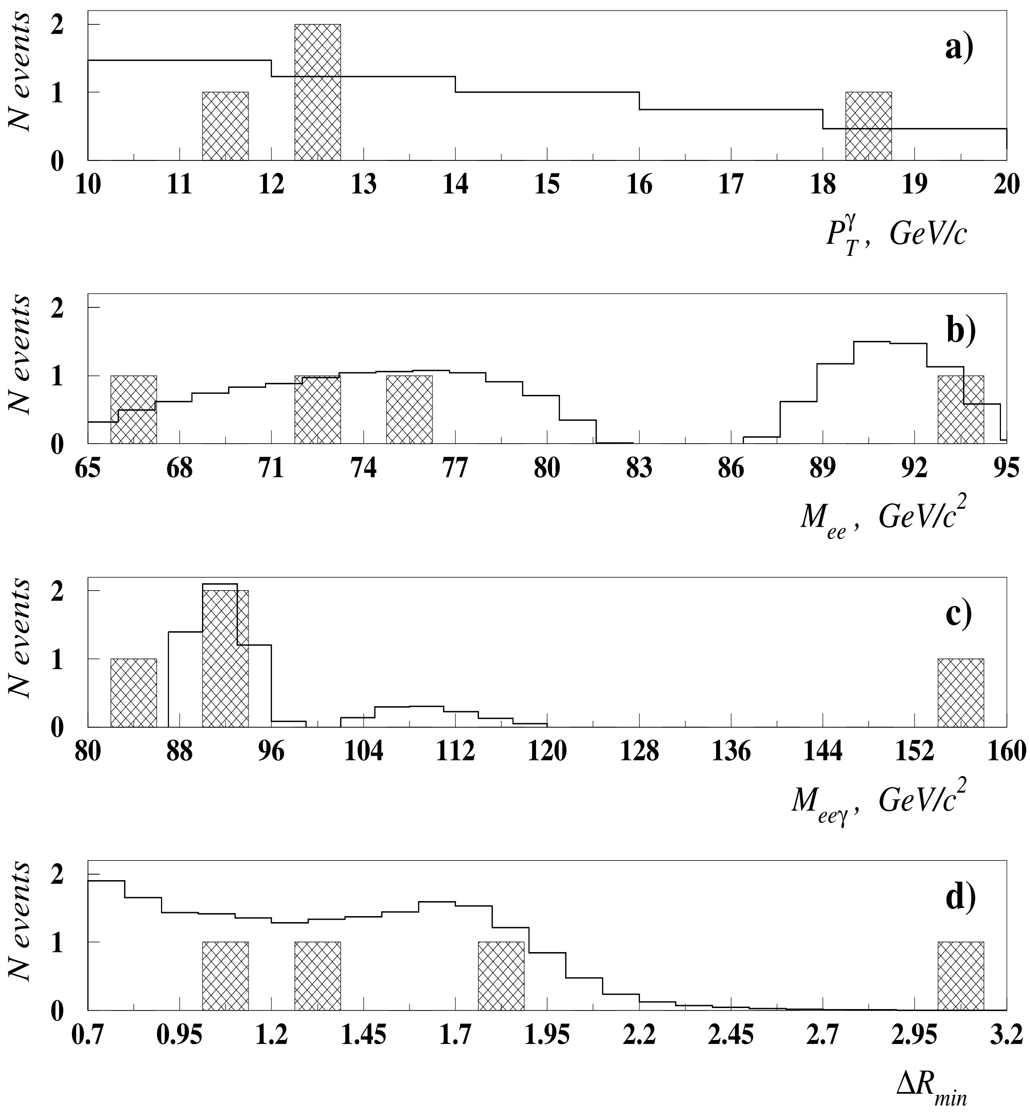

Figure 4.4: Comparison of the parameters of the observed $p\bar{p} \to Z\gamma \to ee\gamma$ candidates and the SM predictions: a) transverse momentum of the photon; b) invariant mass of the electron pair; c) mass of the $ee\gamma$ system; d) minimum separation between the photon and electrons. Hatched bars — observed events; histograms — SM predictions (arbitrary units). The x-axis labels show the bin size for the data points.

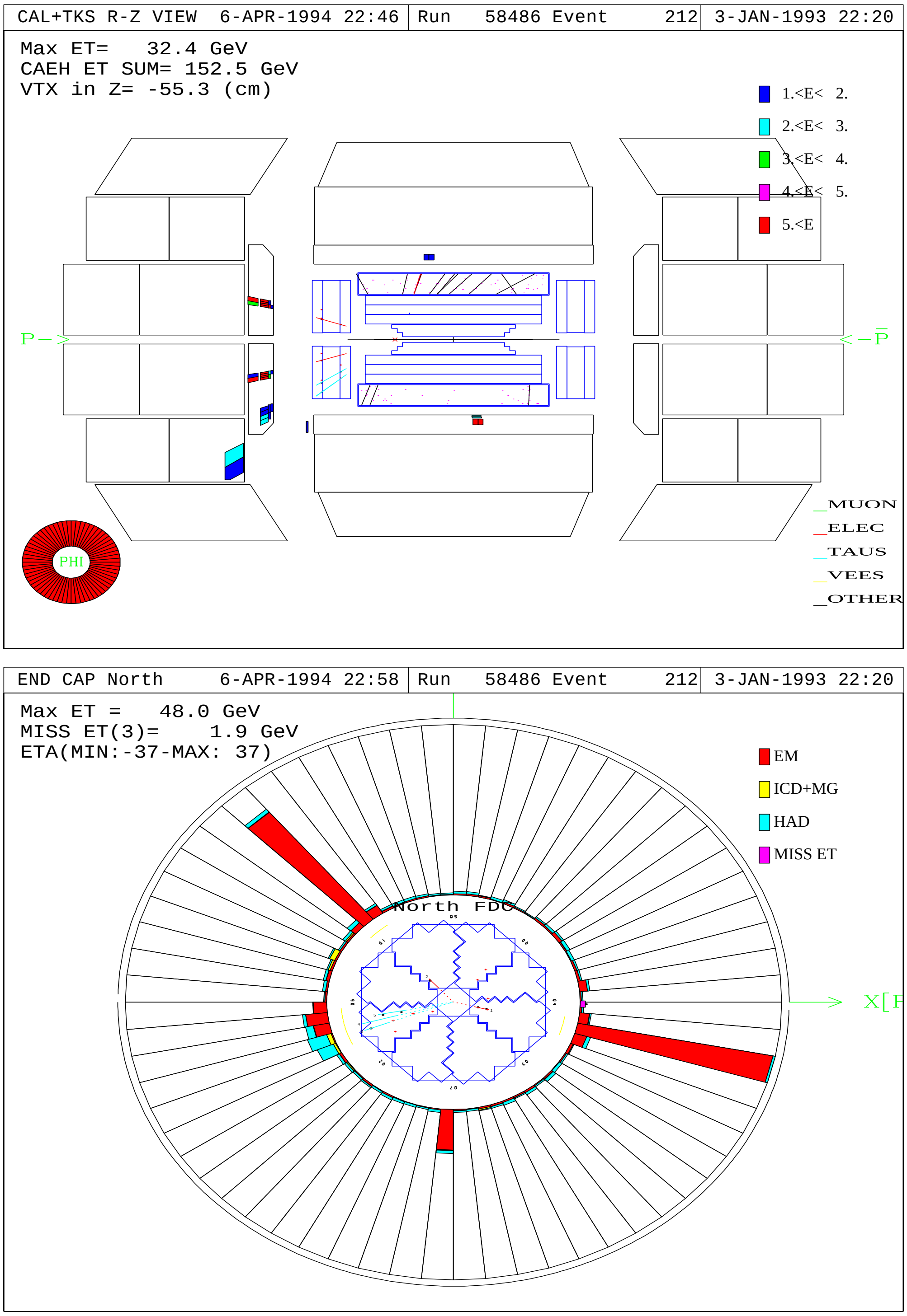

Figure 4.5: Event display of the production $ee\gamma$ candidate. See text.

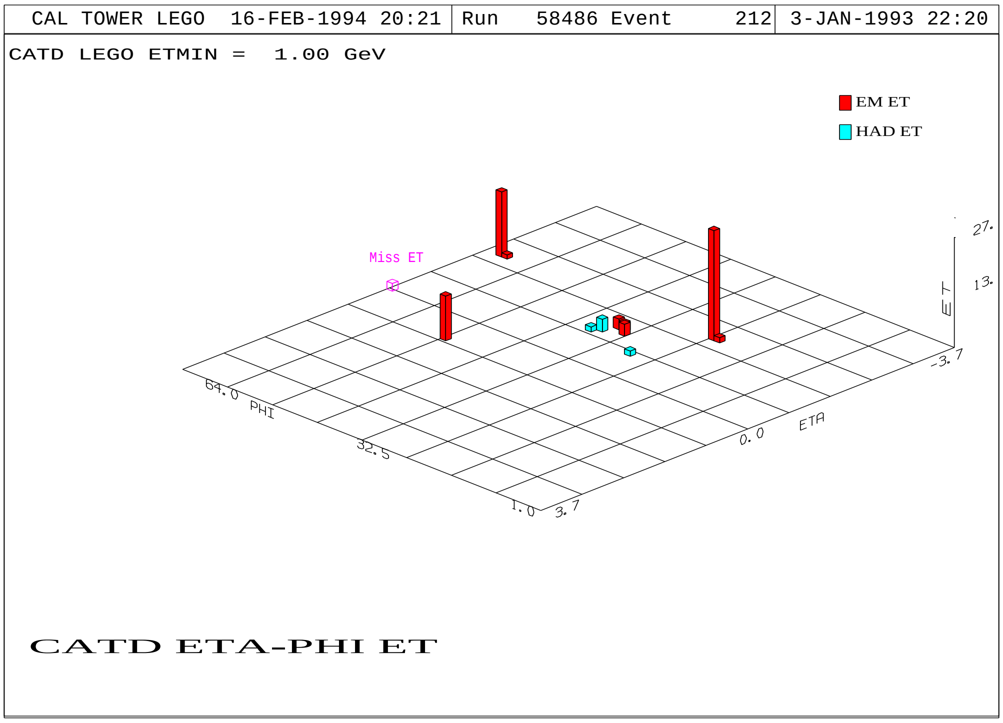

Figure 4.6: Event display of the production $ee\gamma$ candidate (cont'd).

is located just outside the vertex chamber of the detector. The photon is located in the CC (EM cluster in the lower half of the picture). There are no tracks or hits along the line from the vertex to the photon EM cluster. The event also has a jet which can be seen in the lower left part of the picture. It is contained in the forward calorimeter and also deposits some energy in the ICD (see sec. 3.3.6). The bottom plot in Fig. 4.5 shows the end-view of the detector integrated over η_{det} from -3.7 to $+3.7$. The lengths of the filled bars in the calorimeter display of a given event are proportional to the energy depositions. PIXIE displays uncorrected energies; more precise values can be found in Table 4.4. Two electrons with matching FDC tracks are represented by the long bars. The photon is shown as a small bar in the bottom of the plot. The jet is shown as a cluster of filled and hatched bars and a bunch of tracks in the FDC. Finally, the LEGO plot in Fig. 4.6 shows the topology of the event in the $\eta - \phi$ phase space. The vertical scale of the LEGO plot in this figure is proportional to the transverse energy measured in the calorimeter towers. All three electromagnetic clusters are well separated, which is typical for a production event.

4.3 Selection of $p\bar{p} \rightarrow \mu\mu\gamma$ Events

The following set of kinematical and fiducial cuts was used for selection of the reaction (4.2):

$$\begin{gathered} |\eta^{\gamma}_{det}| \leq 1.1 \text{ or } 1.5 \leq |\eta^{\gamma}_{det}| \leq 2.5; \\ |\eta^{\mu^{\pm}}_{det}| \leq 1.0; \quad \Delta R_{\mu^{\pm}\gamma} > 0.7; \\ p_T^{\mu_1} > 15 \text{ GeV}/c, \quad p_T^{\mu_2} > 8 \text{ GeV}/c, \quad p_T^{\gamma} > 10 \text{ GeV}/c. \end{gathered} \tag{4.12}$$

The photon selection cuts are the same as for the $ee\gamma$ case (see sec. 4.2). The acceptance cut for the muons coincide with the η-region covered by the CF (see sec. 3.5). It should be mentioned that the requirement of $\int B\,dl > 1.9$ Tm for one out of two muons essentially squeezes the available $|\eta|$ range for this muon to ≈ 0.8, so we will consider the $\int B\,dl$ cut as a fiducial cut. Different requirements on the momenta of the two muons originate from the fact that the muon momentum resolution (3.6) is modest (see sec. 3.5), and it is even worse for the muon which does not pass the $\int B\,dl > 1.9$ Tm cut (see sec. 4.1.3, Eq. (4.6)). Being asymmetric in p_μ, such a degraded resolution results in a long lower p_μ tail for the reconstructed muon momenta. Furthermore, for radiative Z decays (see sec. 2.3.2) which are expected to dominate for this set of cuts, the momentum of the muon which radiates the photon in the final state will be on average smaller than that for the other muon. Note that the $p_T^\mu > 15$ GeV/c cut is only about one sigma away from the average muon transverse momentum in the Z-decay, which is ≈ 40 GeV/c. This difference in the p_T^μ cuts was properly taken into account by the Monte Carlo calculations of the theoretical cross section (see sec. 3.7).

The so-called "top trigger" (MU_EM) was used for the selection of the candidate sample. This trigger requires one muon with $p_T^\mu > 5$ GeV/c and one electromagnetic cluster with $E_T > 7$ GeV at the Level 2 trigger. By design this trigger requires the muon to be within $|\eta_{det}| < 1.7$ and the electromagnetic tower with $E_T > 7$ GeV (Level 1 trigger). The integrated luminosity collected in run Ia for this trigger is 13.3 ± 1.6 pb^{-1} after correction for bad and special runs (see sec. 3.6.7 for details of the luminosity calculations).

Similar selection criteria applied to the $p\bar{p} \to t\bar{t} \to e\mu + X$ analysis [95, 113] which allowed us to use the very clean sample of 713 events verified by eye-scanning for reconstruction and trigger efficiency studies. This sample contains events with a muon with transverse momentum above 5 GeV/c and an electron/photon with transverse energy above 7 GeV. The efficiency of the single muon trigger was estimated by triggering on the electromagnetic cluster in this sample and counting the number of muon candidates which pass the muon trigger requirements. It was found to be:

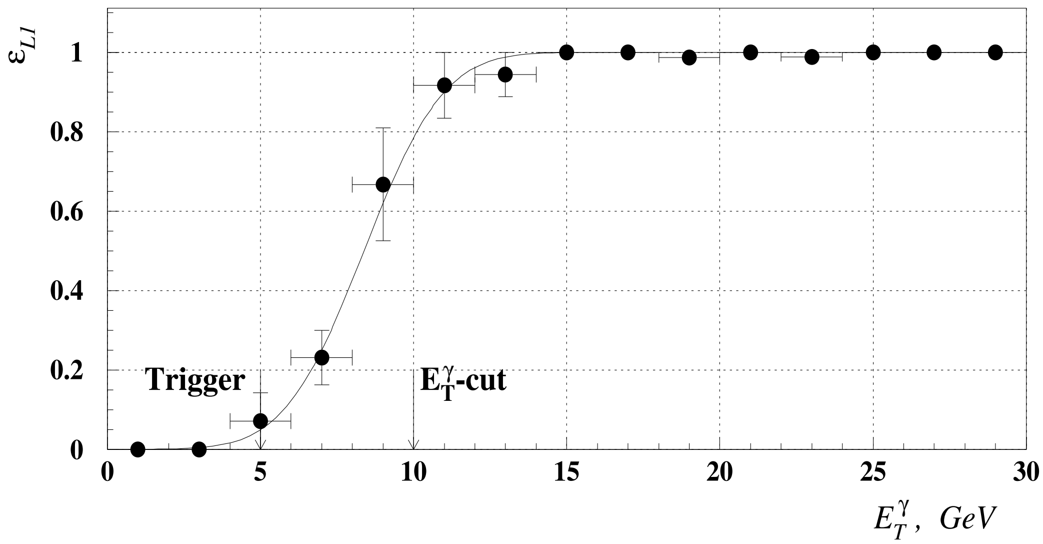

Figure 4.7: Turn-on curve for the Level 1 electromagnetic trigger.

$$\varepsilon_\mu = 0.76 \pm 0.06,$$

independent of muon transverse momentum above 8 GeV/c. This gives the following efficiency for a pair of muons assuming no correlations between muon momenta:

$$\varepsilon^{\mu}_{L1+L2} = \varepsilon_\mu(2 - \varepsilon_\mu) = 0.94^{+0.06}_{-0.09}. \tag{4.13}$$

The efficiency of the photon trigger is governed by the Level 1 trigger turn-on curve shown in Fig. 4.7 [116]. The efficiency is as high as 80% at the p_T^γ offline cutoff (4.12). The trigger is fully efficient for $p_T^\gamma > 14$ GeV/c. The average efficiency for the SM distribution in photon transverse energy is about 97%. The overall p_T^γ-dependent trigger efficiency is taken into account in the Monte-Carlo calculations of the cross section (see sec. 3.7).

The acceptance for the reaction (4.2) was calculated in a similar manner to that for the electron case. For the SM case it is 19%. The overall efficiency and cross section for the reaction (4.2) within the set of cuts (4.12) for the SM case are:

$$\varepsilon_{SM} = 0.064 \pm 0.010; \tag{4.14}$$

$$\sigma_{SM} \cdot \varepsilon_{SM} = 0.184 \pm 0.030 \text{ pb}. \tag{4.15}$$

The whole data set of run Ia was used for event selection. It contains only four non-cosmic events with muons in the CF or EF muon system accompanied by a photon, with all three particles passing the identification and p_T cuts. One out of four events has both muons in the EF system, where the reconstruction efficiency is not yet well understood; furthermore it fails the Level 1 trigger requirements. Another one fails the separation requirement (4.12). The other two events are our final reaction (4.2) candidates. The parameters of these two events are listed in Table 4.5. Both events have no accompanying jets. The muon momentum resolution is quite modest, so the errors on the $M_{\mu\mu}$ and $M_{\mu\mu\gamma}$ are large (of the order of 15 GeV/c^2), and it is challenging to determine if a certain event is due to a production or a decay diagram. However, both events have a low separation between the photon and one of the muons, so most likely they are of the decay type. The large missing transverse energy in these events is most probably due to the poor muon momentum resolution.

The muons in the first event were found to have opposite charges, whereas the muons in the second event have identical charge. However, the efficiency of charge determination is only about 60% for the chosen p_T^{μ} cuts (4.12), so we do not require muons to have the opposite charge.

Particle	Type	p_T	η	ϕ	$\not\!\!E_T$	$M_{\mu\mu\gamma}$	$M_{\mu\mu}$	$\Delta R_{\mu\gamma}$
Run/Event: 58970/2551								
μ_1	2-layer	19.3	-0.23	6.05	19.0	59.1	44.7	0.93
μ_2	low $\int B\,dl$	18.4	0.96	2.94		$(-10.5$	$(-9.4$	3.10
γ		16.0	0.70	6.13		$+31.2)$	$+26.2)$	
Run/Event: 63629/15585								
μ_1	2-layer	26.4	0.14	2.99	30.8	47.0	35.0	0.73
μ_2	low $\int B\,dl$	9.4	-0.83	5.81		$(-5.9$	$(-5.9$	2.93
γ		18.2	-0.31	2.41		$+12.7)$	$+12.0)$	

Table 4.5: Parameters of the final $p\bar{p} \to Z\gamma \to \mu\mu\gamma$ candidates. Unit for masses is GeV/c^2; for transverse momenta — GeV/c; for E_T and $\not\!\!E_T$ — GeV.

Run/Event	$p_T^{\mu_1}$, GeV/c	$p_T^{\mu_2}$, GeV/c	$\not\!\!E_T$, GeV	$M_{\mu\mu}$, GeV/c^2	$M_{\mu\mu\gamma}$, GeV/c^2	χ^2/N_{deg}
58970/2551	18.9	36.4	4.1	62.0	80.6	2.9/2
63629/15585	24.8	37.7	2.4	67.8	87.9	11.2/2

Table 4.6: Parameters of the $\mu\mu\gamma$ candidate events after the kinematical fit.

A simple attempt to correct the low masses of both the dimuon and $Z\gamma$ systems due to the long lower tail of the muon momentum resolution (see Eqs. (3.6), (4.6)) was made. The $\mu^+\mu^-\gamma$ production within the chosen set of cuts (4.12) has a low expected background (see sec. 4.5), so it is assumed that both events are due to the reaction (4.2). Therefore, the missing transverse energy in these events should be very close to zero (likewise the $\not\!\!E_T$ for the $e^+e^-\gamma$ channel, see Table 4.4). Thus we perform a kinematical fit of the event parameters, requiring missing transverse energy to be compatible with zero within the errors (3.5). We assume that muon momenta resolution is the major source of the missing transverse energy mismeasurement. The high and low $\int B \cdot dl$ muon momenta were smeared according to the formulas (3.6) and (4.6), respectively. The corrected parameters of the two candidate events after such a "poor man's fit" are given in Table 4.6. The fit has a reasonable χ^2 per degree of freedom and gives the masses of the $Z\gamma$ system much closer to the Z-mass than that before the fit. The fact that the $\mu^+\mu^-\gamma$ mass after the fit is very close to the Z mass is further evidence in favor of the decay type hypothesis for the two candidate events.

The comparison of the event parameters and the SM predictions is shown in Fig. 4.8. For the dimuon mass (b) and the overall mass distribution (c) the data points are shown both before (hatched bars) and after (filled bars) the constrained fit. The former should be compared with the SM predictions with realistic momentum smearing (solid histograms); the latter should be compared with the unsmeared momenta case (dashed histograms).

The event displays of the first candidate are shown in Fig. 4.9 and 4.10. The top plot in the first figure shows the top view of the full DØ detector. There are two muon tracks pointing to the interaction vertex. One (bottom) track has hits in all 3 layers of the CF; the other one has hits only in the two inner layers, and as is clearly seen from the picture, it hits the gap in the outer layer, which explains the absence of the hits in the outer layer. The three layer track has $\int B\, dl = 1.1$ Tm while the two layer track passes the tight $\int B\, dl$ requirement. The second event has a similar topology. The bottom

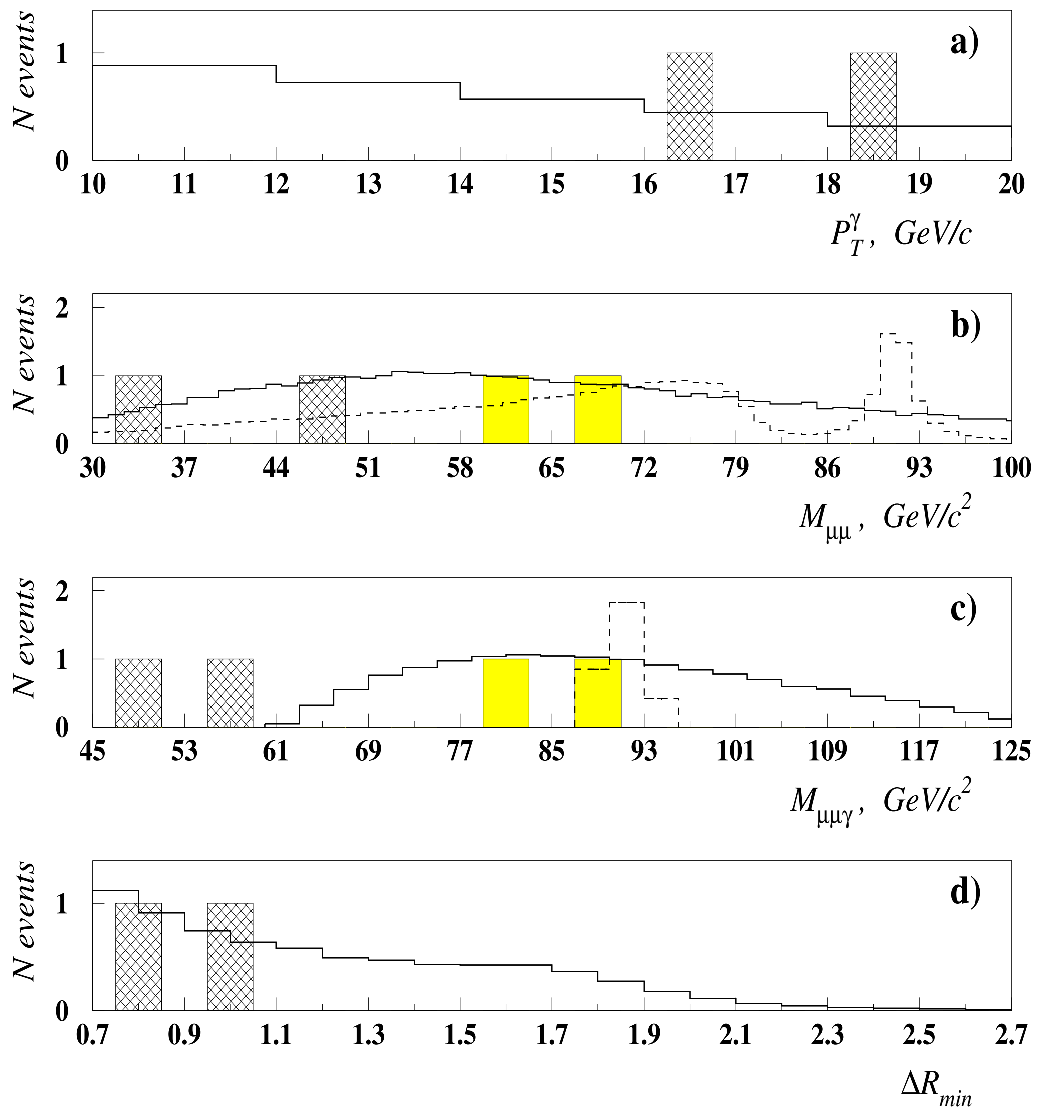

Figure 4.8: Comparison of the parameters of the observed $p\bar{p} \to Z\gamma \to \mu\mu\gamma$ candidates and the SM predictions: a) transverse momentum of the photon; b) invariant mass of the muon pair; c) mass of the $\mu\mu\gamma$ system; d) minimum separation between the photon and muons. Hatched bars — observed events; histograms — SM predictions (arbitrary units). Filled bars — masses after constrained fit which should be compared with the unsmeared distributions shown by the dashed histograms The x-axis labels show the bin size for the data points.

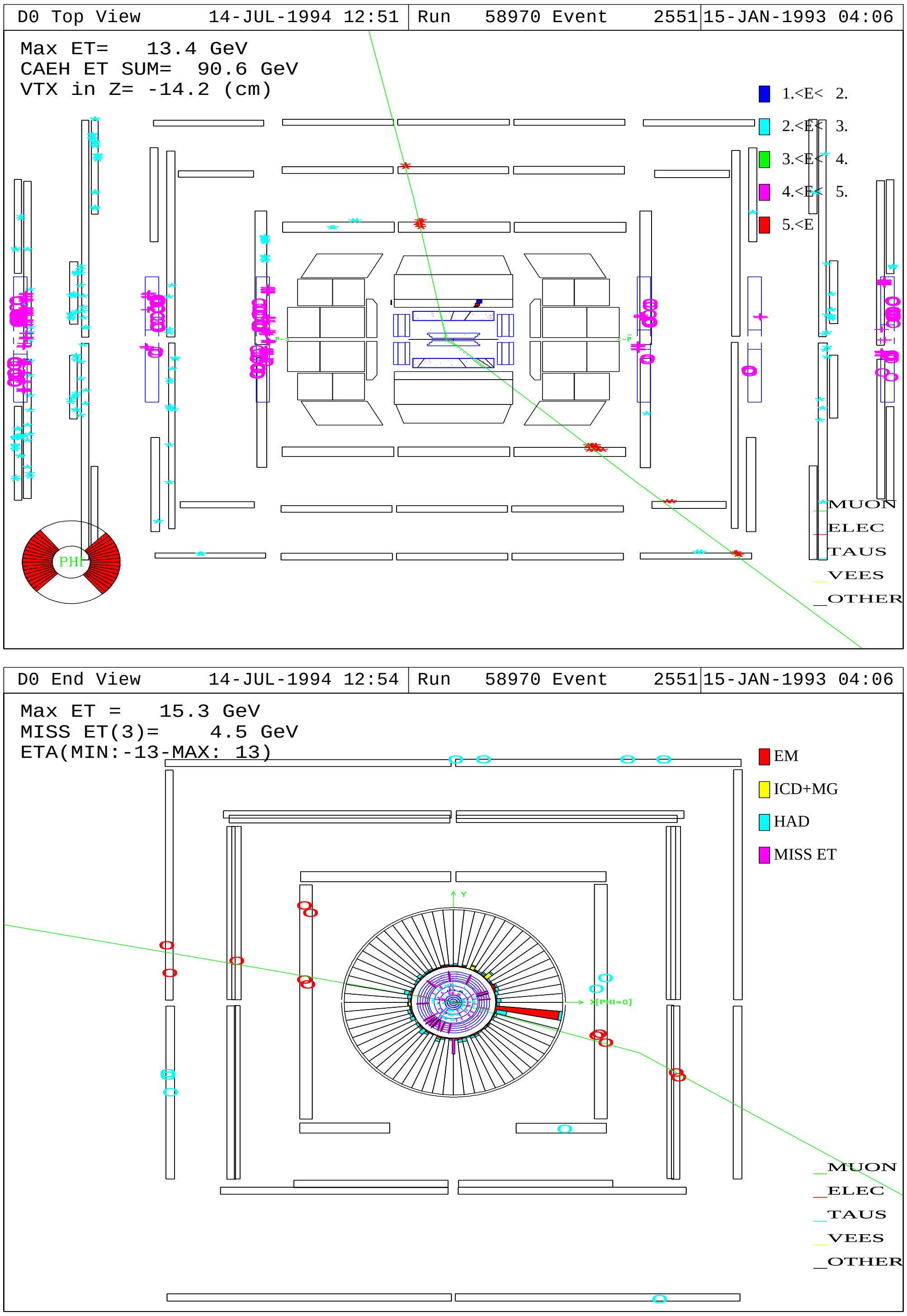

Figure 4.9: Event display of one of the $\mu\mu\gamma$ candidates. See text.

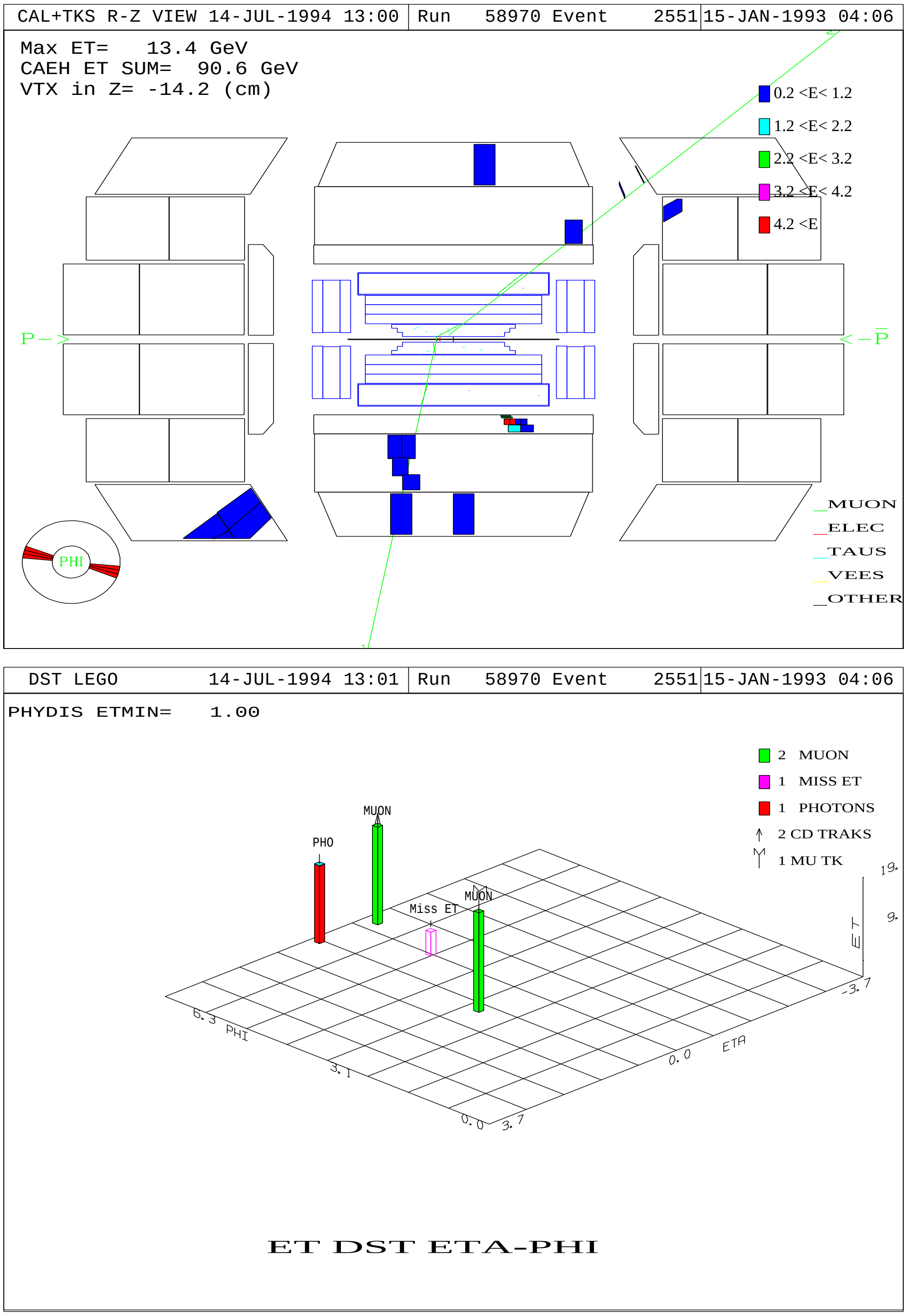

Figure 4.10: Event display of one of the $\mu\mu\gamma$ candidates (cont'd).

plot in the same figure shows the end-view of the detector. A cluster in the electromagnetic calorimeter close in ϕ to one of the muons corresponds to the photon. Both muons and the photon were produced in the same plane in this event, and the $r-z$-view of the corresponding ϕ-slice is shown in the top plot of the second figure. Both the MIP depositions in the calorimeter and the matching tracks in the CDC can be seen for muons. The photon cluster has no close tracks. Finally, the physical $\eta-\phi$ lego-plot is displayed in the bottom of the second figure. It shows the population of the phase space with the final state particles. The photon is clearly close to one of the muons as is expected for decay events (see Fig. 2.7).

4.4 Selection of $p\bar{p} \rightarrow \nu\nu\gamma$ Events

Currently we do not use the neutrino channel for establishing limits on the anomalous couplings or to state an observation of signal, but certain attempts to detect $Z\gamma$ events in this channel were made.

The advantages of the neutrino decay mode of Z were discussed in sec. 2.3.3. The theoretical backgrounds to this channel due to the $Z+jets$ and multijet production are expected to be acceptable for $p_T^\gamma > 30$ GeV/c. Therefore we attempted to select $p\bar{p} \rightarrow \nu\bar{\nu}\gamma$ candidates using the following cuts:

$$p_T^\gamma > 30 \text{ GeV}/c, \quad \not{E}_T > 30 \text{ GeV}, \tag{4.16}$$
$$|\eta_{det}^\gamma| < 1.1 \text{ or } 1.5 < |\eta_{det}^\gamma| < 2.5.$$

The ELE_MAX Level 2 trigger can be used for selecting these events. This trigger requires an isolated EM-cluster with $E_T > 20$ GeV which passes certain quality cuts which are less stringent than the standard photon identification cuts, and a missing transverse energy in the calorimeter above 20 GeV. This trigger follows the Level 1 EM_1_MAX trigger which requires an EM-cluster with transverse energy above 14 GeV. Both Level 1 and Level 2 triggers were not prescaled during the run Ia. They are used for the $p\bar{p} \to W \to e\bar{\nu}$ analysis.

However, most of the events which pass the selection criteria (4.16) are due to the direct production of W's which subsequently decay into electron-antineutrino pairs: $p\bar{p} \to W \to e\bar{\nu}$, with the electrons being misplaced into the PPHO (photon) banks due to the tracking inefficiency. There are about 9,000 $W \to e\bar{\nu}$ events with a "tight" electron passing the standard electron identification cuts (see sec. 4.1.1), and with $E_T^e > 30$ GeV, $\not\!\!E_T > 30$ GeV. Taking into account the tracking efficiency of $\approx 87\%$ (see Table 4.1), one would expect about 1500 $W \to e\bar{\nu}$ events with the electron misplaced in the PPHO bank and passing all our cuts. The expected cross section of the reaction (2.9) within the set of cuts is about 0.5 pb (assuming $\approx 60\%$ overall detection efficiency), which corresponds to 7 signal events. In order to make the background at least comparable with the signal one needs an additional rejection of the fake process $W \to e\bar{\nu} \to \gamma \not\!\!E_T$ by about a factor of 100.

Recent studies show that the main tracking inefficiency in the CDC (see sec. 3.4.3) is due to a poor reconstruction of the z-coordinates of the hits. In the VTX chamber (see sec. 3.4.1) the main reason is a high number of hits, which results in ambiguities in combining them into tracks. The same problem exists for the FDC (see sec. 3.4.4) where the density of tracks is much higher than that in the central region. Therefore, the tracking inefficiency is primarily due to poor track finding, and not because of problems with hit reconstruction. As a part of the work on the neutrino channel candidate selection it was shown that an additional rejection power for electrons of about 15 with a 70% efficiency for photons can be achieved by counting the density of hits in 3-dimensional and 2-dimensional tracking roads. The specialized package, HITSINFO [117], was developed and released as part of DØRECO for this purpose. Utilization of the TRD (see sec. 3.4.2) information should improve this rejection even further.

p_T^γ and $\not{E}_T$ thresholds	Standard selection			With hit-counting		
	N_{SM}	N_{anom}	N_{bck}	N_{SM}	N_{anom}	N_{bck}
30 GeV/c	6.4	28	1340	4.5	20	89
40 GeV/c	3.6	25	203	2.5	18	14
45 GeV/c	2.7	24	45	1.9	17	3

Table 4.7: Expected number of SM (N_{SM}), anomalous ($h_{40}^Z = 0.5$, N_{anom}), and $W \to e\bar{\nu}$ background (N_{bck}) events for the standard e/γ identification criteria and after applying the hit counting electron rejection method.

Utilization of the HITSINFO package does not solve the background problem completely — the background is still higher than the signal. However, for the case of anomalous couplings the cross section is much larger than that for the SM case, especially for large values of p_T^γ. Table 4.7 shows the expected number of signal events for the SM case, for the anomalous coupling $h_{40}^Z = 0.5$ and form factor scale $\Lambda = 500$ GeV (which corresponds to our current 95% confidence level (CL) limit from combined electron and muon channel, see Chapter 5), and the expected $W \to e\bar{\nu}$ background before and after applying the hit counting algorithm. It is clear that for transverse momenta above 45 GeV/c the sensitivity to anomalous couplings is very high, and the anomalous signal is 5 times higher than the expected background. Therefore, the p_T^γ-fit method (see sec. 5.2) with the correct background shape should be capable of setting even better limits on the anomalous couplings in the neutrino channel than those obtained using the charged decay modes of the Z (provided, that no significant excess of high p_T^γ events above the background level is observed, likewise for the electron and muon channels).

Work in this direction is under way, and the hope is that it will be possible to obtain the limits on the anomalous $Z\gamma$ production in the reaction (2.9) in the near future.

4.5 Backgrounds

In this section we describe the main sources of background in the $e^+e^-\gamma$ and $\mu^+\mu^-\gamma$ channels.

4.5.1 QCD Background

The major source of background to $\ell^+\ell^-\gamma$ signal is the QCD background due to $\ell^+\ell^- + jets$ (dominated by $Z + jets$) production with one of the jets faking a photon by fragmenting into a high energy π^0 which subsequently decays into a pair of spatially close photons unresolved in the EM calorimeter.

For the $e^+e^-\gamma$ channel there is an additional background from jets faking electrons. Jets are able to fake electrons by fragmenting into a leading π^0, with the additional track originating either from photon conversion or from soft charged particles accompanying the π^0.

This type of background dominates also for several other processes, e.g. $p\bar{p} \to W\gamma \to \ell\bar{\nu}\gamma$ or direct photon production ($j\gamma$). The quantitative characteristics of this background depend very much on the details of the detector design, jet definition algorithms, etc. For the DØ detector the probability of a jet faking an electron/photon was studied in great detail [118].

Jets Faking Electrons or Photons

The method used for estimating the probability that a jet fakes an electromagnetic cluster is based on measuring the fraction of n $jet(s) + \gamma$ events in the $(n+1)$ $jets$ sample $(n = 1, 2, ...)$. Here γ is a PPHO bank which passes all photon identification criteria (see Table 4.1). This method is based on the assumption that all photons in such a sample are in fact QCD fakes. This is not exactly true because of direct photon production [119]. We will discuss the direct photon contamination in the background sample later.

The initial data set for fake probability studies was collected during the same physics run using several jet triggers. Because of the very high multijet production cross section most of these triggers were prescaled (see sec. 3.6.2) which results in several dips at the trigger thresholds in the E_T^γ spectrum. In order to eliminate this trigger bias we consider only multijet events with the photon which is not a leading particle. We also perform the analysis separately in CC and EC, and restrict the fiducial volume to $|\eta^{\gamma}_{det}| < 1.1$ in CC and $1.5 < |\eta^{\gamma}_{det}| < 2.5$ in EC, which coincides with the fiducial volume used for both the $e^+e^-\gamma$ and $\mu^+\mu^-\gamma$ analyses (see cut definitions (4.8) and (4.12)).

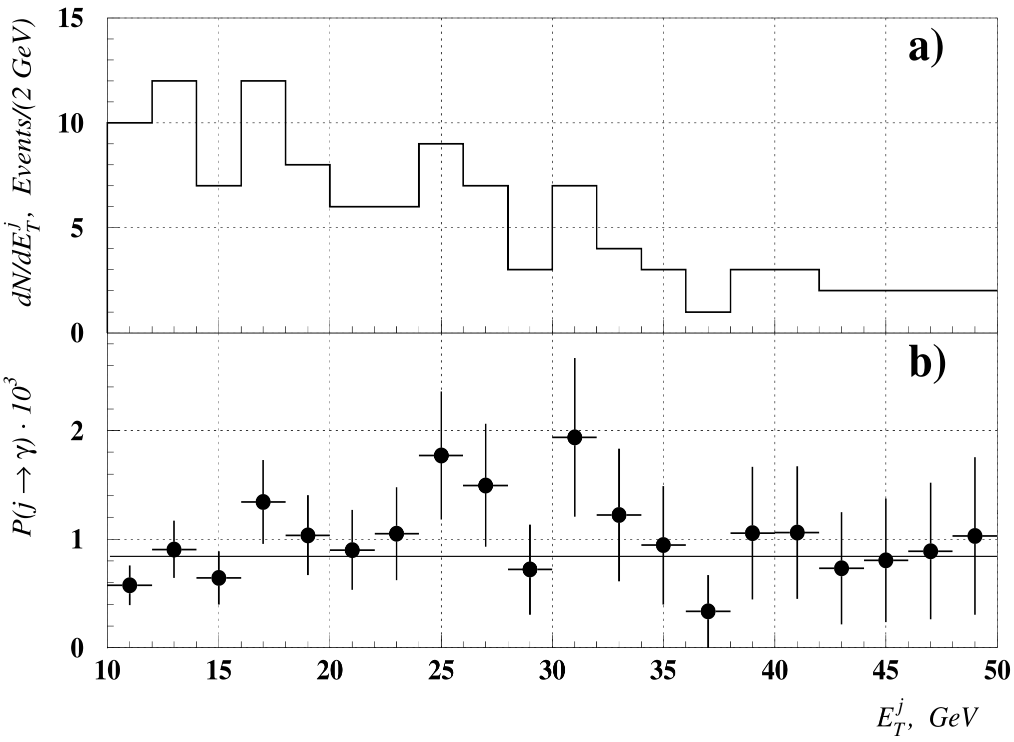

Figure 4.11: a) E_T spectrum of non-leading CC photons in the multijet sample passing standard photon identification and selection cuts; b) jet faking photon probability in the CC as a function of jet/photon transverse energy.

The transverse energy spectrum of the CC photons accompanying jets is shown in Fig. 4.11 (a). The probability of a jet faking a photon is obtained by dividing the E_T spectrum of fake photons by that of the non-leading jets in pure multijet events, and is shown in Fig. 4.11 (b) for the CC. It is well fitted by either a linear or constant function. The same is true for the fake background in the EC. For this analysis we use constant fake probabilities. The uncertainties due to the fit method are included in the total systematics of the background estimates.

The same method was used for obtaining the probabilities for a jet faking a "tight" or a "loose" (i.e. passing "loose" electron/photon cuts, and failing at least one of the "tight" electron cuts, see sec. 4.1.1) electron (in what follows e_t and e_ℓ, respectively) with transverse momenta above 25 GeV/c in the central and end calorimeters. The fake probabilities are summarized in Table 4.8. The fourth column of the table shows the fake probabilities averaged over the detector using the observed ratio of the CC/EC jets (3/1). The systematic uncertainties of these probabilities are dominated by the low statistics of the fake jets and are of the order of 15%. The probability to fake any electron is given by the sum of the probabilities to fake a "tight" and a "loose" electron, as shown in the bottom row of the table.

Faking	CC	EC	Average	Direct γ corrected
$j \to \gamma$	0.84 ± 0.08	0.90 ± 0.11	0.86 ± 0.09	0.65 ± 0.18
$j \to e_t$	0.62 ± 0.07	1.5 ± 0.2	0.84 ± 0.10	0.84 ± 0.10
$j \to e_\ell$	1.7 ± 0.1	1.6 ± 0.2	1.7 ± 0.1	1.5 ± 0.2
$j \to e$	2.3 ± 0.1	3.1 ± 0.3	2.5 ± 0.1	2.3 ± 0.2

Table 4.8: Probabilities (in units of 10^{-3}) for a jet to fake a photon or electron in the DØ detector.

The last column of the table represents a rough way to take into account the direct photon contamination in the multijet sample used for the analysis.

Recent DØ results on direct photon cross section [119] show that the fraction of direct photons passing the photon selection cuts used in this analysis in the p_T^γ range of 10 to 50 GeV/c (where most of the background is concentrated) is $25 \pm 25\%$. The large (systematic) error is due to the big uncertainty on the direct photon cross section, especially in the low p_T^γ region. The probability of a direct photon to fake a PELC (electron) bank is negligible at our level of accuracy because such a photon must either convert before the tracking chambers or be quite close to a random track in the central detector. The probability in both cases is of the order of 10%. Thus, accounting for the direct photon contamination decreases the probability for a jet to fake a photon (by $25 \pm 25\%$) or a "loose" electron ($13 \pm 13\%$). The correction is less for the "loose" electrons since only about half of them are found in PPHO (photon) banks. The fake probabilities after the direct photon corrections are listed in the last column of Table 4.8.

QCD Background in the Electron Channel

Now we are ready to estimate the QCD background in the electron channel. It is important to estimate this background from the data, because this ensures that all possible sources of the background, including double and triple jet fakes are weighted with the correct factors in the estimate.

It is convenient to break the background into three parts and treat them independently. The first background originates from $e^+e^- + jets$ (dominated by $Z + jets$) with one of the jets faking a photon with transverse momentum above 10 GeV/c. Using real $e^+e^- + jets$ data and multiplying the number of jets by

$P(j \to \gamma)$ (see Table 4.8) is the most precise way of estimating this contribution to the background, since the real $e^+e^- + jets$ sample already contains possible contamination from multijet events with two jets faking electrons. The sample used for the estimation of this background contains one "tight" and another, "tight" or "loose," electron with transverse energy above 25 GeV each. Both electrons are required to pass the standard electron selection criteria (see sec. 4.1.1 and 4.2). We also required a separation $\Delta R_{ej} > 0.7$ between the jet and both of the electrons, in the same way we required the electron-photon separation for the signal. There are 225 CC ($|\eta_{det}| < 1.1$) and 79 EC ($1.5 < |\eta_{det}| < 2.5$) jets with $E_T^j > 10$ GeV in this sample. Multiplying the number of the jets by $P(j \to \gamma)$ from Table 4.8 (the last column) we obtain the following number of events for the first component of the QCD background: $N_1^B = 0.20 \pm 0.05$.

The second and the third components of the QCD background are due to jets faking electrons. In order to calculate these backgrounds we use the $e_t + \gamma + jets$ and $e_\ell + \gamma + jets$ events. The requirement on the electron (photon) is to pass the standard tight or loose identification criteria and a transverse energy cut of 25 (10) GeV. In addition, the photon must have separations $\Delta R_{\gamma j}, \Delta R_{\gamma e} > 0.7$ from the electron and the jet. These two samples contain the $e^+e^- + jets$ events with one electron being misidentified as a photon and also the multijet background with two jets faking an electron and photon. (Because of the low transverse energy cut on the photon, the samples are dominated by the mixture of $Z + jets$ and Drell-Yan e^+e^- pairs with associated jet production)

Selection of these events is quite different from that for the signal events, because one can not use the parent $Z \to ee$ sample due to a low E_T cut on one of the electromagnetic clusters. Thus, we had to reprocess about 75% of run Ia statistics with the requirement of the ELE_HIGH trigger (one electromagnetic cluster with E_T above 20 GeV at the Level 2 trigger) in order to select the $e_{t/\ell}+\gamma+jets$ events. The normalization factor taking into account the different trigger and the fact that only a part of the run Ia statistics was processed, is 1.21. It was calculated by comparing the number of the e^+e^-+jets events with $E_T^e > 25$ GeV in the standard $Z \to ee$ sample and in the background sample. The number of CC (EC) jets with $E_T^j > 25$ GeV observed in the background sample for $e_t+\gamma+jets$ topology is 54 (26); for $e_\ell+\gamma+jets$ topology, 59 (27). The fiducial volume used for counting jets in CC/EC is the same as that for the first component of the background.

At this point extra caution is necessary because simple multiplication of the number of jets by faking probabilities and the normalization factor would result in a double-counting of the multijet background with all three electromagnetic objects being jet fakes, since this background was already estimated as a part of the N_1^B. Although the effect of double counting is small, it was decided to subtract the multijet component from the background samples. This can be achieved by comparing the number of events in the $e_t+\gamma+jets$ and the $e_\ell+\gamma+jets$ samples using the "loose/tight" electron ratio given by equation (4.4) and the probabilities for faking "loose"/"tight" electrons. A simple calculation shows that the numbers of the multijet fakes in the background samples with the jet in CC/EC are 8/6 for the $e_t+\gamma+jets$

topology, and 26/12 for the $e_\ell + \gamma + jets$ topology. Therefore, we base our background calculations on 46/20 (33/15) $e_t{+}\gamma{+}jets$ ($e_\ell{+}\gamma{+}jets$) events with jets in CC/EC. Multiplication of these numbers by the normalization factor and $P(j \to e_{t/l})$ gives the following number of the background events of the second and third components of the QCD background: $N_2^B + N_3^B = 0.23 \pm 0.03$ events. (This number should be compared with 0.31 ± 0.03 events without subtraction of the multijet fraction from the background samples, which proves that the double-counting does not change results significantly).

The total QCD background in the $e^+e^-\gamma$ channel is:

$$N^e_{QCD} = N_1^B + N_2^B + N_3^B = 0.43 \pm 0.06. \tag{4.17}$$

The p_T spectrum of the background was obtained by combining the p_T spectrum of jets contributing to the first component of the background and the p_T spectra of photons in the events contributing to the second and third components of the background. The subtraction of the double-counted multijet contribution was done simply by scaling the p_T^γ spectra. Since the effect of such a subtraction translates into only one standard deviation of the total background, this approximation is sufficiently accurate. The p_T^γ spectrum of the QCD background is shown in Fig. 4.12 (a). The enhancement at ≈ 50 GeV/c is due to the Jacobian peak [120] in the transverse energy spectrum of the electrons with a missing track in the $Z + jets \to ee + jets \to e\gamma + jets$ events. This spectrum was fitted by the sum of an exponential function $C \cdot e^{-(\alpha p_T + \beta p_T^2)}$ describing rapidly falling jet E_T spectrum, and a Gaussian (to approximately account for the bump at 50 GeV/c).

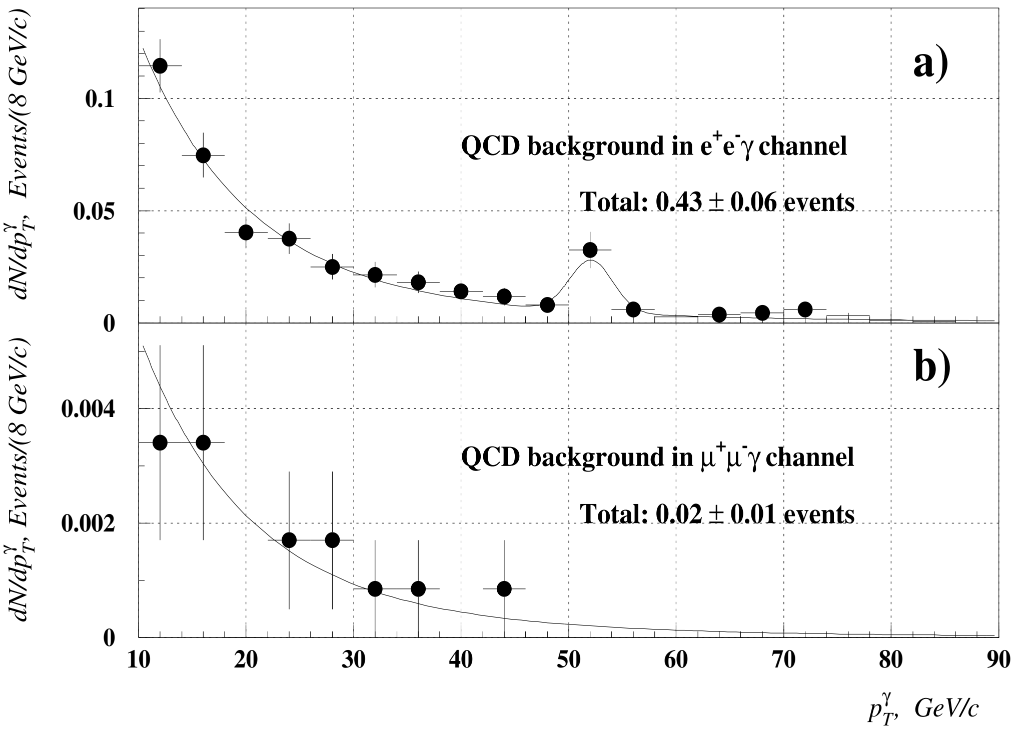

Figure 4.12: a) QCD background in the $e^+e^-\gamma$ channel. The bump around 50 GeV/c is due to the Jacobian peak from the $Z + jets$ production with a jet faking an electron and one of the electrons from the Z-decay being misidentified as a photon. b) QCD background in the $\mu^+\mu^-\gamma$ channel. For fit definitions see text.

QCD/Cosmic Background in the Muon Channel

The QCD background calculation in the muon channel is much simpler since the probability for jets to fake a pair of muons is negligible. Such a fake in principle can occur for b-jets, but the requirement of muons well isolated from jets (see sec. 4.1.3) together with the transverse momentum cut (4.12) suppresses this type of fakes to zero.

The estimation of the QCD background is based on the $\mu^+\mu^- + jets$ sample with muons passing the standard selection cuts (see sec. 4.1.3 and 4.3). We also require a separation of $\Delta R_{\mu j} > 0.7$ between the jet and either of muons, similar to the photon-muon separation requirement for the signal. This sample includes Drell-Yan with associated jet production, $Z + jets$, and cosmic background events. Therefore, the estimation of the background from the data automatically takes into account the background from cosmic rays overlapping with multijet events. (This background is already small because of the muon quality cuts.) The other type of cosmic background with the muon radiating a high energy photon in the detector material (external *bremsstrahlung*) is negligible [121] due to the requirement of a large separation ($\Delta R_{\mu\gamma} > 0.7$) between the photon and both muons.

The background sample was selected using a single muon trigger which requires a 15 GeV/c muon at Level 2. The prescale factor for this trigger, if compared with the trigger used for the signal selection (see sec. 4.3) was calculated to be 1.3$\pm$0.3. The number of jets with a transverse energy above 10 GeV in the CC ($|\eta_{det}| < 1.1$) and EC ($1.5 < |\eta_{det}| < 2.5$) is 8 and 7, respectively. Multiplication of these numbers by the prescale factor and $P(j \rightarrow \gamma)$ (Table 4.8, last column) gives the following number of QCD/cosmic background events:

$$N^{\mu}_{QCD} = 0.02 \pm 0.01. \tag{4.18}$$

The p_T spectrum of the background is shown in Fig. 4.12 (b). It was fitted with the function $C \cdot e^{-(\alpha p_T + \beta p_T^2)}$. Due to poor background statistics we used the values of α, β obtained for the electron channel.

4.5.2 $Z \to \tau\tau$ Background

Another source of "background" to $p\bar{p} \to Z\gamma \to \ell^+\ell^-\gamma$ is a cascade decay of Z into neutrinos and a dimuon or dielectron pair through the τ-lepton channel: $Z \to \tau^+\tau^- \to \nu_\tau\nu_\ell\bar{\nu}_\tau\bar{\nu}_\ell\ell^+\ell^-$. Although such cascade decay events are not really background events, they are still not included in the DØBAUR Monte Carlo, so one must make sure that the contribution of the cascade decays is taken into account when comparing the theoretical and experimental cross sections and deriving limits.

From the branching ratio for the $\tau \to \ell\bar{\nu}_\ell\nu_\tau$ decay (0.178 ± 0.003 [9]), the fraction of such decays is $3.2 \pm 0.1\%$. It is further reduced by the p_T cuts on the final state leptons. The exact fraction of τ-events was calculated by comparing the number of events passing the lepton selection cuts in the $Z \to \ell^+\ell^-$ and $Z \to \tau^+\tau^- \to \nu_\tau\nu_\ell\bar{\nu}_\tau\bar{\nu}_\ell\ell^+\ell^-$ samples generated using the ISAJET Monte Carlo [104] and the DØGEANT detector simulation program [103]. It was shown that the expected fractions of the cascade τ-decay events in the e and μ signal samples are:

$$f_e = (0.10 \pm 0.05)\%; \quad f_\mu = (1.4 \pm 0.5)\%, \tag{4.19}$$

where the error is dominated by the systematic error due to the different E_T spectra of leptons in the $p\bar{p} \to Z \to \ell\ell$ decays and in the $p\bar{p} \to Z\gamma \to \ell\ell\gamma$ reactions. This background can be safely neglected for the electron channel.

4.6 Signal

Using the observed number of events in each channel and the background estimates (4.17), (4.18), (4.19), we obtain the following expectations for the number of signal events in the $e^+e^-\gamma$, $\mu^+\mu^-\gamma$ and $\ell^+\ell^-\gamma$ channels:

$$S_{ee\gamma} = 3.57^{+3.15}_{-1.91} \pm 0.06; \tag{4.20}$$

$$S_{\mu\mu\gamma} = 1.95^{+2.62}_{-1.29} \pm 0.01; \tag{4.21}$$

$$S_{\ell\ell\gamma} = 5.52^{+3.56}_{-2.37} \pm 0.06. \tag{4.22}$$

Here the first error is a symmetric conservative 68% CL error, based on Poisson statistics [122] (see sec. 5.1 for more details on the error definitions), and the second one is the systematic error of the background estimate.

These formulas represent the most important result of this work — the first observation of $Z\gamma$ production in hadron collisions[1].

The SM predicts the following number of events (calculations are done with the DØBAUR generator, see sec. 3.7, and formulas (4.11), (4.15)):

$$S^{SM}_{ee\gamma} = 3.2 \pm 0.3 \pm 0.4; \tag{4.23}$$

$$S^{SM}_{\mu\mu\gamma} = 2.5 \pm 0.4 \pm 0.3; \tag{4.24}$$

$$S^{SM}_{\ell\ell\gamma} = 5.6 \pm 0.7 \pm 0.7. \tag{4.25}$$

Here the first error is due to the MC systematics (see sec. 3.7) and the second one is due to the 12% luminosity uncertainty. The SM predictions are in

[1]Recently the CDF Collaboration also observed 8 $Z\gamma$ events [5] in the 1992–1993 data.

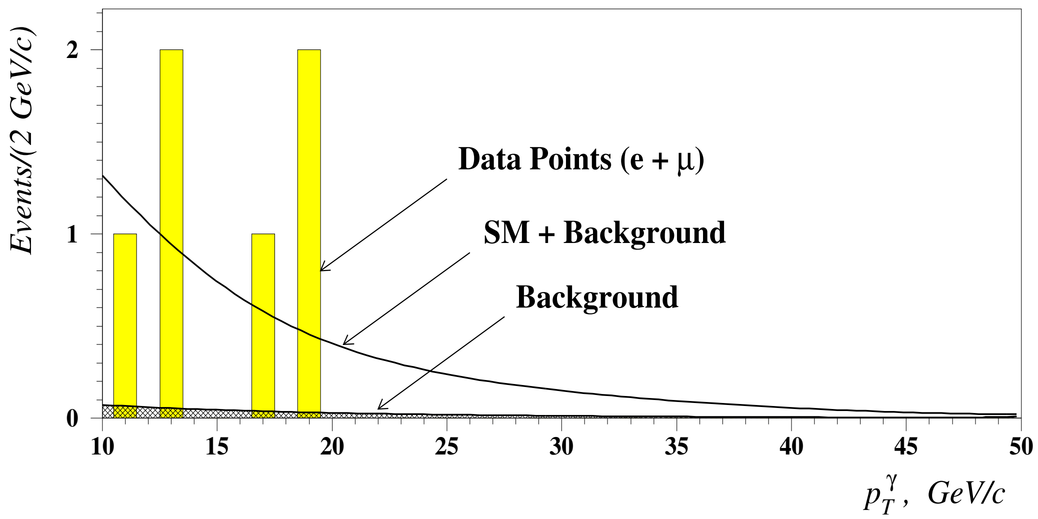

Figure 4.13: Comparison of the observed p_T^γ spectrum of the combined $ee\gamma$ and $\mu\mu\gamma$ signal and the SM predictions. Shadowed bars show data points; hatched curve represents overall background; solid curve shows sum of the SM predictions and background.

good agreement with the observed signal. There is no evidence for anomalous couplings which result in an increase of the expected number of events (see sec. 2.3.2).

The combined p_T^γ spectrum of the $e^+e^-\gamma$ and $\mu^+\mu^-\gamma$ events is shown in Fig. 4.13. The background and the SM prediction are shown in the same plot. The total background is about 6%. Again, the data are in good agreement with the SM expectation and there is no evidence for production of high-p_T^γ events typical of anomalous couplings (see sec. 2.3.2).